

Geochemical Controls on Uranium Release from Neutral-pH Rock Drainage Produced by Weathering of Granite, Gneiss, and Schist

Elliott K. Skierszkan ^{1,*}, John W. Dockrey ², K. Ulrich Mayer ¹, Viorica F. Bondici ³,
Joyce M. McBeth ⁴ and Roger D. Beckie ¹

¹ Department of Earth, Ocean and Atmospheric Sciences, University of British Columbia, 2020–2207 Main Mall, Vancouver, BC V6T 1Z4, Canada; umayer@eoas.ubc.ca (K.U.M.); rbeckie@eoas.ubc.ca (R.D.B.)

² Lorax Environmental Services Ltd., 2289 Burrard St, Vancouver, BC V6J 3H9, Canada; john.dockrey@lorax.ca

³ Canadian Light Source Inc., 44 Innovation Blvd, Saskatoon, SK S7N 2V3, Canada; ibi.bondici@lightsource.ca

⁴ Department of Geology, University of Regina, 3737 Wascana Parkway, Regina, SK S4S 0A2, Canada; joyce.mcbeth@uregina

* Correspondence: eskiersz@eoas.ubc.ca

S1. Detailed Methods of Power X-Ray Diffraction Analyses

Synchrotron powder diffraction measurements of the drill-core samples used in the kinetic tests were conducted using the Macromolecular Crystallography beamline (CMCF-BM) at the Canadian Light Source. CMCF-BM is a bending magnet beamline with a Si(111) double crystal monochromator. The samples were ground and loaded into 1.5 cm long, 0.032 inch polyimide capillary tubes and sealed at both ends with Loctite 454 Prism gel epoxy. Diffraction data of the samples, an empty capillary, and a lanthanum hexaboride (LaB₆) standard were collected at 18 KeV energy of the incident beam (wavelength of 0.68878 Å) and with a Rayonix MX300HE detector at a distance of 200 mm. The standard was used to calibrate the sample–detector distance, detector centering, and detector tilt. Background was subtracted using the pattern obtained from the empty capillary sample. The 2D X-ray diffraction patterns were calibrated and integrated using GSASII software [70]. The calibration parameters obtained were applied to the entire pattern before integration. Mineral phases were identified by matching the diffraction patterns of the samples to the patterns of the reference single-phase mineral. The Inorganic Crystal Structure Database was used in combination with X'Pert HighScore Plus (PW3212) software. Elemental abundance ICP-MS data were taken into consideration for the identification of the main phases present in the samples. Rietveld refinement calculations [71] were conducted on the data to provide quantitative estimates of the identified mineral abundances in the samples.

S2. Sequential Chemical Extraction Protocol and Results

Sequential chemical extractions were conducted by SGS Minerals using 1 g of pulverized rock and five extraction steps, based on an adaptation of the method of Tessier et al. [56]:

- 1—15 mL 1 M Nanopure™ distilled water;
- 2—15 mL 1 M MgCl₂;
- 3—15 mL 1 M Na-acetate (adjusted to pH 5.0 with acetic acid);
- 4—15 mL 0.04 M NH₂OH-HCl (in 25% v/v acetic acid);
- 5—15 mL aqua regia.

Leachates were analyzed by ICP-MS and ICP-OES at SGS.

S3. Additional Supplementary Figures and Tables

Table S1. Overview of kinetic test experiments and solid-phase composition of rocks used in tests.

Lithology Facies		Gneiss			Schist			Granite	
		Oxide	Transition	Fresh	Oxide	Transition	Fresh	Transition	Fresh
Column ID		C5-GnO	C6-GnT	--	C3-ScO	C4-ScT	--	C13-GrT	C14-GrF
Field bin ID		FB-GnO	FB-GnT	FB-GnF	FB-ScO	FB-ScT	FB-ScF	FB-GrT	FB-GrF
Total-S	wt. %	0.016	0.083	0.21	0.031	0.10	0.42	0.035	0.045
Sulfide-S	wt. %	0.01	0.07	0.18	0.01	0.05	0.35	0.005	0.03
TIC	wt. %	0.23	0.48	0.66	0.94	1.58	2.09	0.01	0.11
NPR	[]	38	15	8.4	81	42	13	0.7	6.5
U	µg/g	5.5	6.3	6.1	2.6	2.7	3.2	7.6	6.2
U-SFE [§]	µg/g	0.032	0.032	0.030	0.0038	0.022	0.014	0.0014	0.0057
Fe	wt. %	1.5	1.2	1.8	2.9	2.6	2.9	0.87	1.1
Fe oxides*	mol Fe/kg	0.56	0.24	0.62	1.97	0.26	0.20	0.40	0.22
Sulfide minerals*, †	wt. %	< dl	0.11	0.29	< dl	0.07	0.42		
Carbonate minerals**	wt. %	0.0	4.3	3.0	9.7	10.6	24.4	< dl	< dl
HFO [‡]	mol/kg		0.0038		0.031	0.0034			

Column Sequencing Experiments

Phase 1: cycles 1 to 99

All columns irrigated with distilled-deionized H₂O

Phase 2: Feeding schist effluent into gneiss columns (cycles 100 to 105)

Effluent from C4-ScT was used to feed C6-GnT

Effluent from C3-ScO was used to feed C5-GnO

Phase 3: Feeding gneiss effluent into schist columns (cycles 105 to 135)

Effluent from C6-GnT was used to feed C4-ScT

Effluent from C3-GnO was used to feed C3-ScO

Note: * Fe oxide and sulfide mineral abundances determined by QEMSCAN. ** Carbonate minerals identified by XRD include: calcite, ankerite, dolomite, and Mg-calcite. † Sulfide minerals identified by XRD include: pyrite, arsenopyrite, and arsenian pyrite. ‡ Hydrous ferric oxide (HFO) availability calibrated in PHREEQC (See Supporting Information, Section S.3.1). § U-SFE = mass of shake-flask extractable U.

Table S2. Geochemical reactions added to the wateq4f.dat database for PHREEQC simulations.

Reaction	log K	Reference
<i>Aqueous complexation</i>		
$2\text{Ca}^{2+} + \text{UO}_2^{2+} + 3\text{CO}_3^{2-} \rightleftharpoons \text{Ca}_2\text{UO}_2(\text{CO}_3)_3$	30.7	Dong and Brooks [24]
$\text{Ca}^{2+} + \text{UO}_2^{2+} + 3\text{CO}_3^{2-} \rightleftharpoons \text{CaUO}_2(\text{CO}_3)_3^{2-}$	27.18	Dong and Brooks [24]
$\text{Mg}^{2+} + \text{UO}_2^{2+} + 3\text{CO}_3^{2-} \rightleftharpoons \text{MgUO}_2(\text{CO}_3)_3^{2-}$	26.11	Dong and Brooks [24]
<i>Sorption reactions</i>		
$\text{HFO_wOH} + \text{CO}_3^{2-} + \text{H}^+ \rightleftharpoons \text{HFO_wOCO}_2^- + \text{H}_2\text{O}$	12.78	Mahoney et al. [58], Appelo et al. [72]
$\text{HFO_wOH} + \text{CO}_3^{2-} + 2\text{H}^+ \rightleftharpoons \text{HFO_wOCO}_2\text{H} + \text{H}_2\text{O}$	20.37	Mahoney et al. [58], Appelo et al. [72]
$\text{HFO_sOH} + \text{UO}_2^{2+} \rightleftharpoons \text{HFO_sOUO}_2^+ + \text{H}^+$	3.736	Mahoney et al. [58]
$\text{HFO_wOH} + \text{UO}_2^{2+} \rightleftharpoons \text{HFO_wOUO}_2^+ + \text{H}^+$	2.534	Mahoney et al. [58]
$\text{HFO_wOH} + \text{UO}_2^{2+} + \text{CO}_3^{2-} \rightleftharpoons \text{HFO_wOUO}_2\text{CO}_3^- + \text{H}^+$	9.034	Mahoney et al. [58]
$\text{HFO_wOH} + \text{UO}_2^{2+} + 2\text{CO}_3^{2-} \rightleftharpoons \text{HFO_wOUO}_2(\text{CO}_3)_2^{3-} + \text{H}^+$	15.28	Mahoney et al. [58]
$\text{HFO_wOH} + \text{UO}_2^{2+} + \text{H}_2\text{O} \rightleftharpoons \text{HFO_wOUO}_2\text{OH} + 2\text{H}^+$	-5.111	Mahoney et al. [59]

Table S3. Uranium redox speciation determination by XANES-LCF using uranyl nitrate and uraninite as U(VI) and U(IV) standards, respectively.

Sample ID	Lithology	Weathering Facies	U ($\mu\text{g/g}$)	U(IV) (%)	U(VI) (%)	R-factor
KAM144308	Gneiss	Oxide	30	0	100	0.0038
KAM029385	Schist	Oxide	25	11	89	0.0142
KAM079346	Schist	Transition	22	53	47	0.0059
KAM091516	Gneiss	Transition	41	83	17	0.0058
72146B	Gneiss	Transition	11	51	49	0.063
Composite	Fresh	Waste	6	33	67	0.025
KAM047252	Schist	Fresh	40	72	28	0.0134
KAM078808	Gneiss	Fresh	15	73	27	0.0137

Table S4. Mineralogy of rocks used in kinetic tests determined by pXRD.

Sample ID	GnO*	GnT*	GnF*	ScO*	ScT*	ScF*	GrT**	GrF**
Lithology	Gneiss	Gneiss	Gneiss	Schist	Schist	Schist	Granite	Granite
Weathering	Oxide	Transition	Fresh	Oxide	Transition	Fresh	Transition	Fresh
Mineral	wt. %	wt. %	wt. %	wt. %	wt. %	wt. %	wt. %	wt. %
<i>Carbonates</i>								
Ankerite				2.3				
Calcite			2.3		10.6	5.1		
Dolomite		3.6		3.5		14.4		
Magnesium calcite		0.7	0.7	3.9		4.9		
<i>Total Carbonates</i>	0	4.3	3	9.7	10.6	24.4	0	0
<i>Sulfides</i>								
Arsenopyrite		0.5						
Pyrite		0.2	0.2	0.4	0.2	1.3		
<i>Total Sulfides</i>	0	0.7	0.2	0.4	0.2	1.3	0	0
<i>Silicates</i>								
Albite	11.3	8.4	22.3		18.5	12.8	18	22
Anorthite							6.7	9.8
Biotite					9.1	5.7	0.7	1.4
Diopside					6.2			
Grossular					7.8			
Kaolinite	10.2	9.6	9.3	13.3	5.1	6.8	7	4.4
Magnesiohornblende					3.3			
Microcline	22	16.2	14.1	5.1		11.8	27	29
Muscovite	10.4	9	12.5	10.9			5.7	4.6
Orthoclase					11.1			
Phengite		1.9		7.3		7.2		
Phlogopite								
Quartz	46.2	49.9	38.5	53.2	28.2	29.8	35	29
<i>Total silicates</i>								
<i>Sulfates</i>								
Barite						0.3		

Note: *XRD analyses conducted at the Canadian Light Source. **XRD analyses conducted by SGS Minerals.

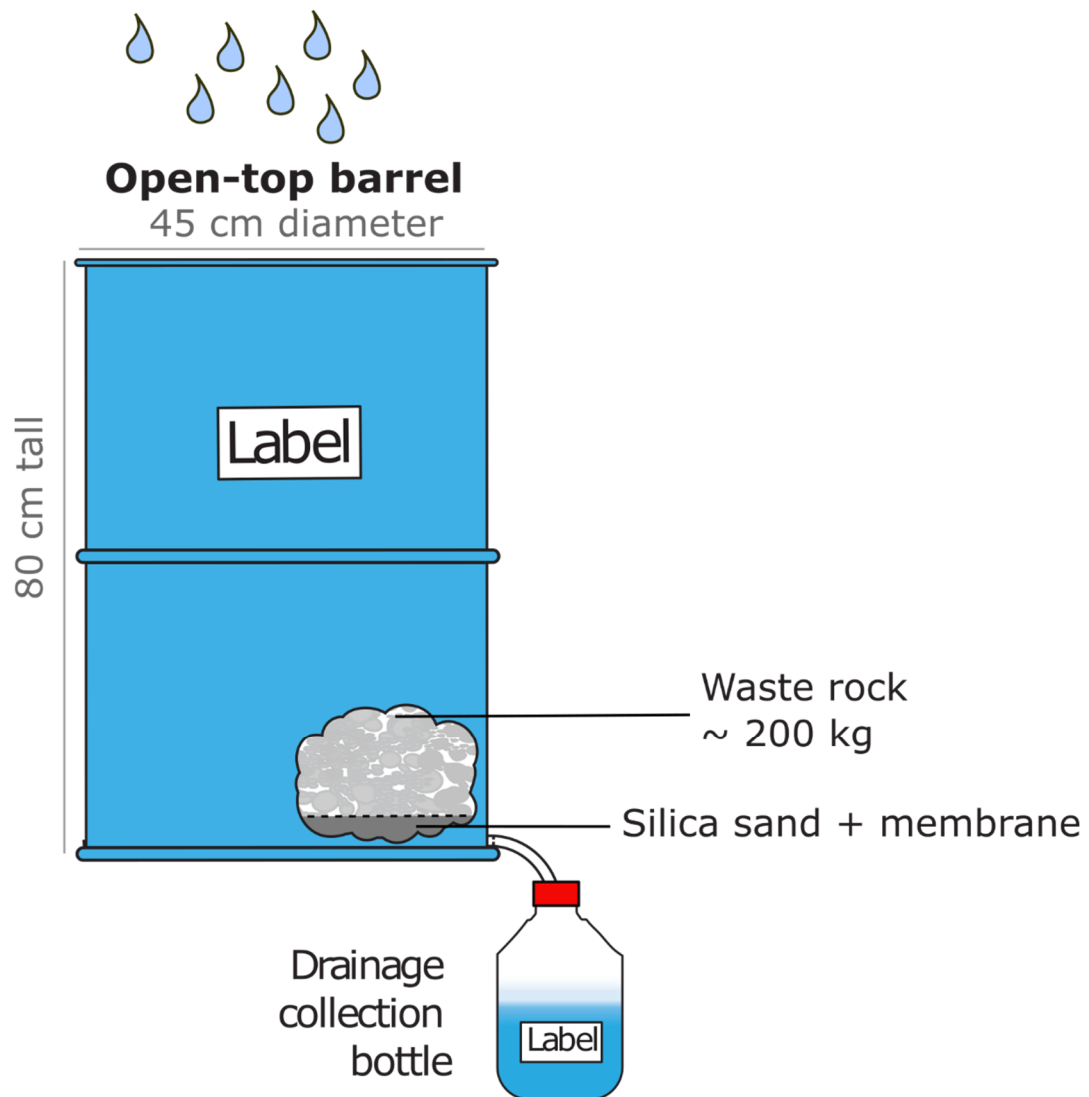


Figure S1. Schematic diagram of field-bin experiment apparatus, which consists of a large HDPE barrel filled with waste rock and exposed to weathering under local climatic conditions. Modified from Vriens et al., *Chemosphere* 215,858-869(2020).

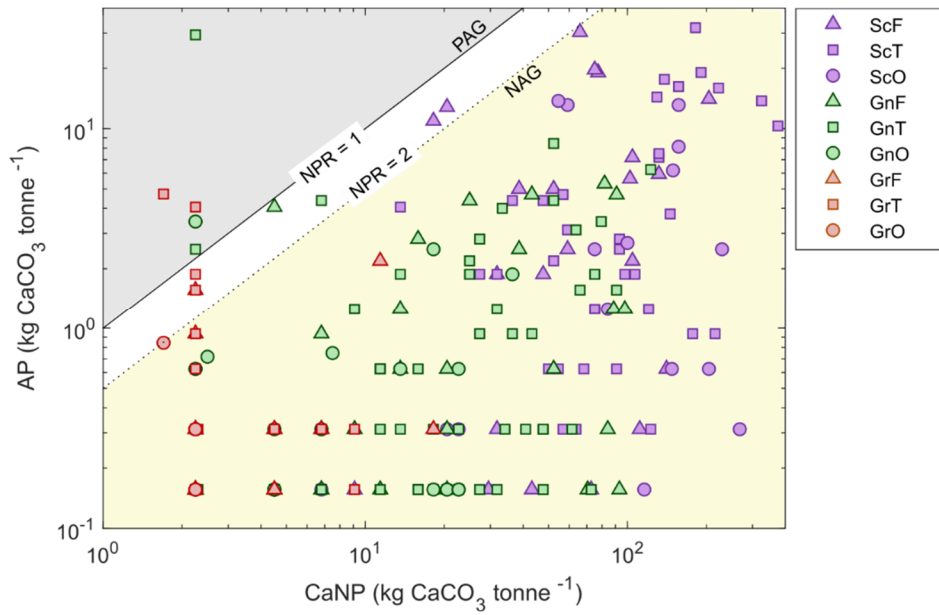


Figure S2. Acid-generating potential (calculated from total sulfur) against carbonate neutralizing potential (calculated from TIC) showing that the majority of rock in the Coffee deposit is non-acid-generating and that NPR characteristics are generally in the order schist > gneiss > granite.

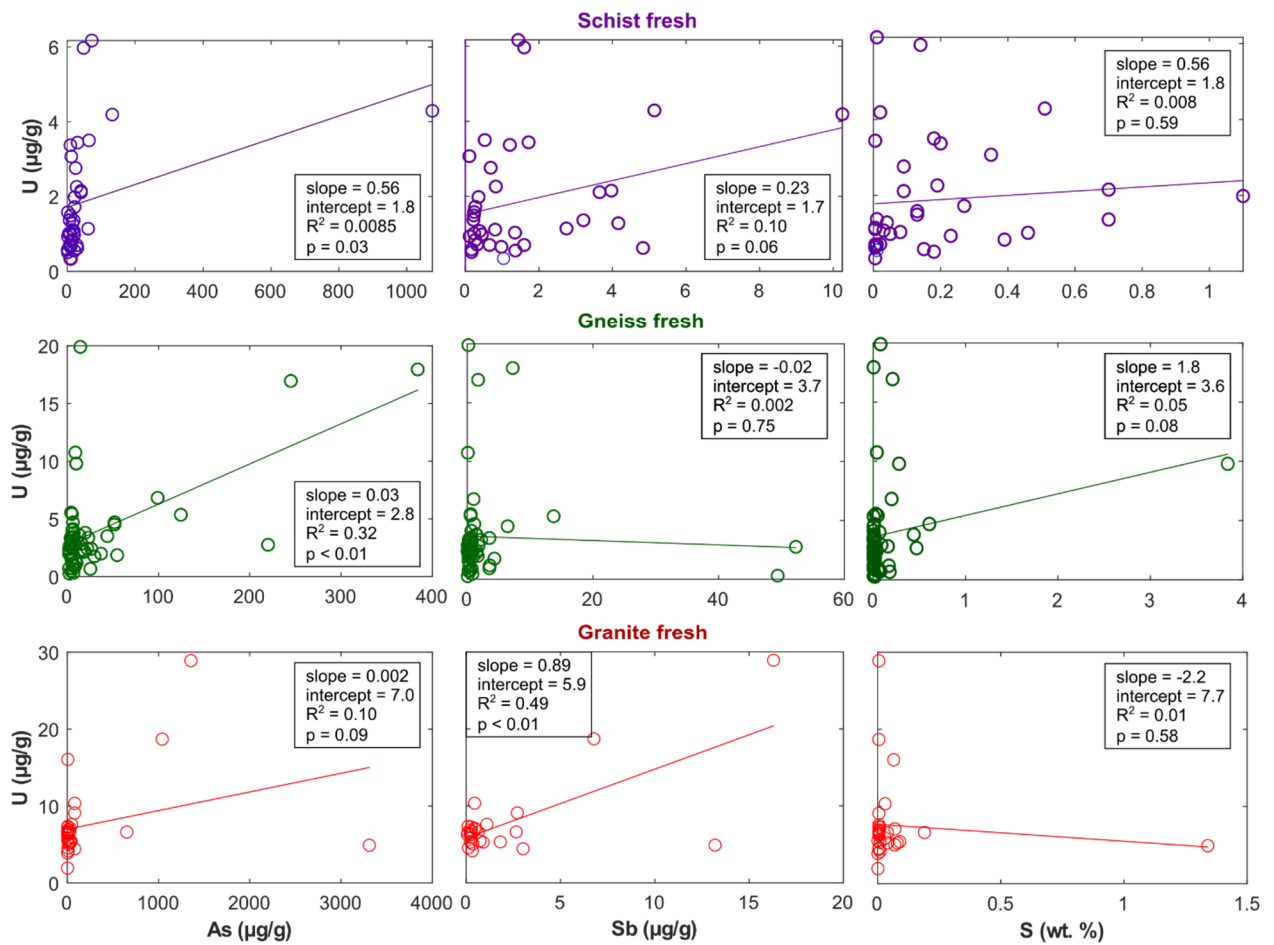


Figure S3. Bivariate plots of U against As (left), Sb (middle), and S (right) by rock type for Coffee drill-core samples from the fresh weathering facies.

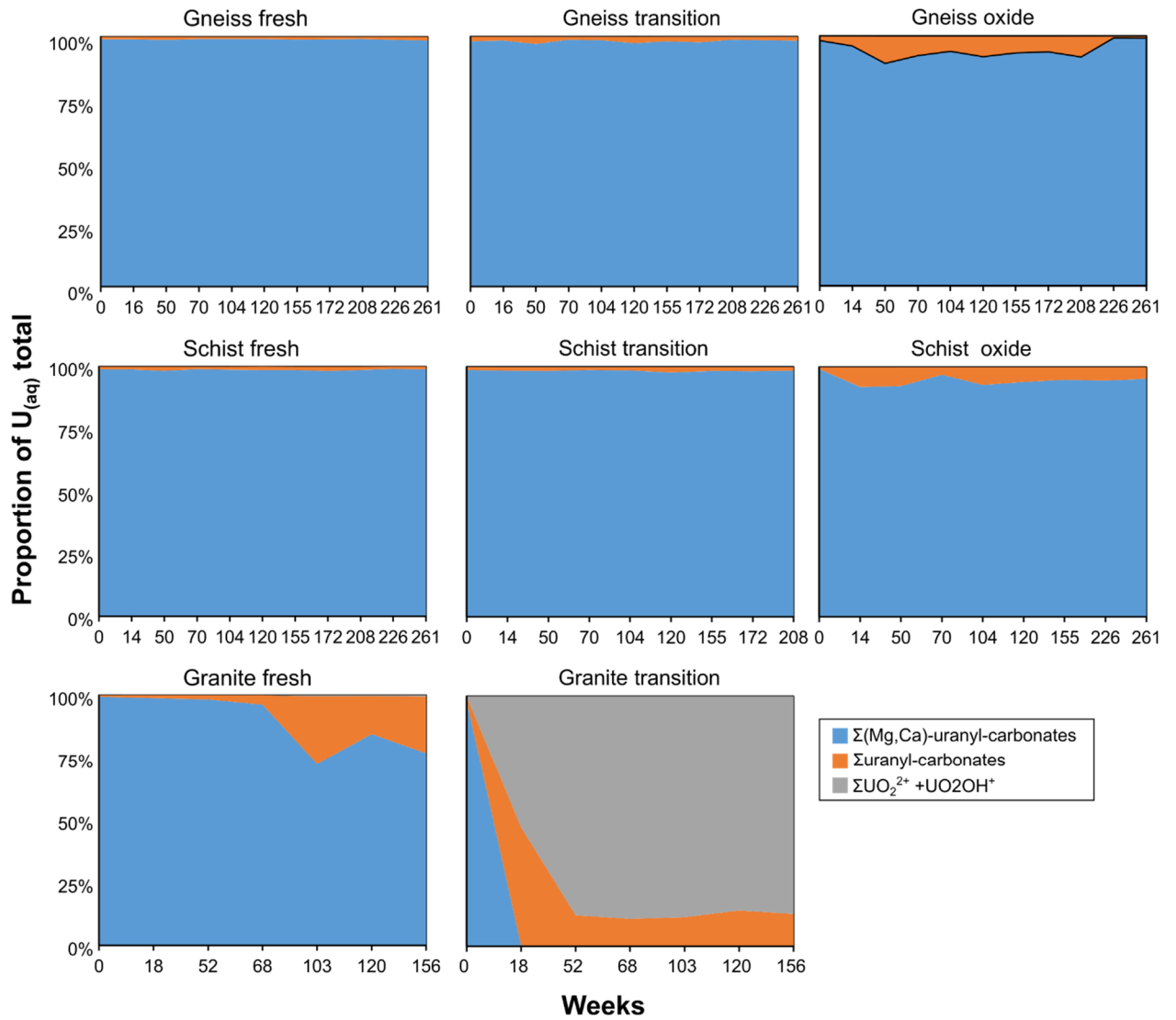


Figure S4. Aqueous U speciation in field-bin leachates. $\Sigma(\text{Mg,Ca})\text{-uranyl-carbonates} = \text{CaUO}_2(\text{CO}_3)_2^{2-} + \text{Ca}_2\text{UO}_2(\text{CO}_3)_2 + \text{MgUO}_2(\text{CO}_3)_2^{2-}$; $\Sigma\text{uranyl-carbonates} = \text{UO}_2\text{CO}_3 + \text{UO}_2(\text{CO}_3)_2^{2-} + \text{UO}_2(\text{CO}_3)_3^{4-} + \text{UO}_2(\text{CO}_3)_4^{6-}$.

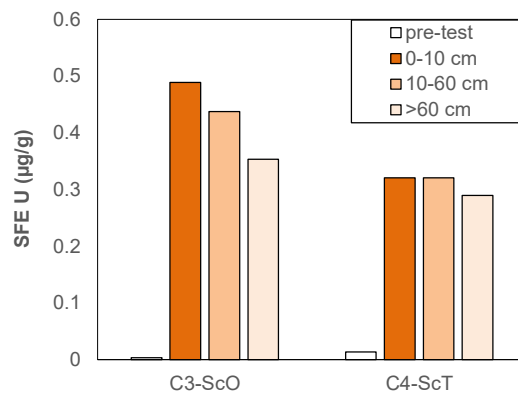


Figure S5. Uranium recovered by shake-flask extractions (SFE) in schist columns. White bars indicate SFE recovery before column experiments. Darker colors indicate SFE-recoverable U over three depth

intervals in column residues at the end of the experiments: 0–10, 10–60, and 60 cm to the bottom of the column.

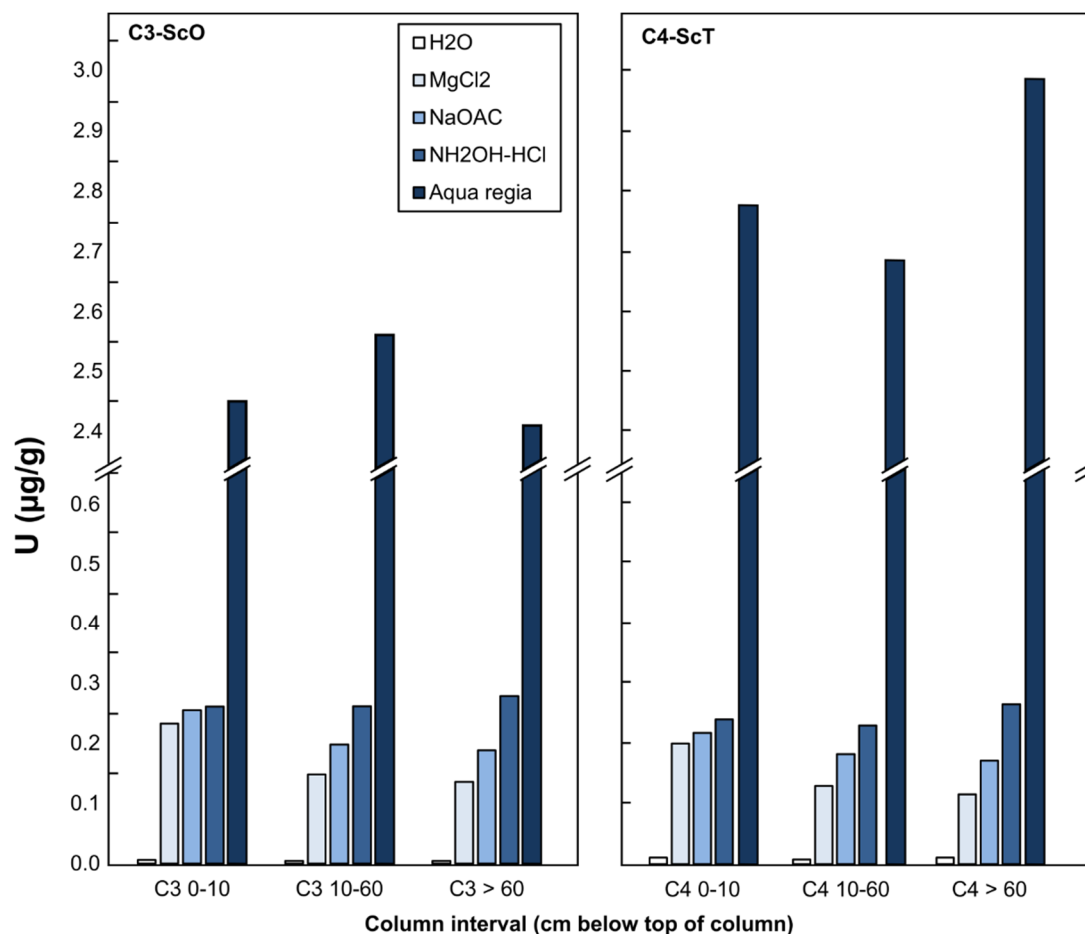


Figure S6. Sequential chemical extraction results for residues at the end of experiments in the schist oxide (left) and schist transition (right) columns.

S4. PHREEQC Model Description for Simulation of Column Experiments

S4.1 Step 1: Calibration of HFO Availability in the Schist Oxide, Schist Transition, and Gneiss Transition Columns Using Phase 1 Data.

HFO availability was calibrated in column experiments using a series of batch reactions representing each sample from each column in Phase 1, prior to the sequencing experiments conducted in Phases 2 and 3. In each batch reaction, U(VI) was added into a system containing HFO and the measured aqueous concentrations (without U) and pH, allowing the U to equilibrate between the solution and the HFO. This process is visually presented (Supplementary Figure S7) and described in detail below.

The mass of “mobile” U(VI) added in each simulation was estimated as a proportion of the measured solid-phase U abundance in the rocks used in the respective columns based on sequential-chemical extraction (SCE) data. The proportion of total U that was released during SCE steps 1 to 4 (step 1 to 4 reagents described in Supplementary Information, Section S.2, above) was assumed to be available for sorption-desorption reactions and was therefore used as the input of U(VI) mass in the PHREEQC model. Because SCE were only applied to column residues at the end of the experiments, we used a mass-balance approach to infer the mass of U that was associated with SCE steps 1 to 4, “ M_{initial} ”, prior to the column experiments:

$$M_{\text{initial}} = M_{\text{final}} - M_1 - M_2 + M_3 \quad (1)$$

where:

- M_{initial} is mass of U recovered in SCE steps 1 to 4 at the start of column experiments (inferred parameter);
- M_{final} is the measured mass of U in SCE steps 1 to 4 at the end of column experiments (measured parameter);
- M_1 is the mass of U lost as effluent between cycles 1 and 105, i.e., during Phase 1 and before schist columns received gneiss influent solution;
- M_2 is the mass of U lost as effluent during Phase 3, i.e., from cycle 105 to the end of the experiment;
- M_3 is the mass of U entering schist columns as gneiss influent solution during Phase 3, i.e., from cycle 105 to the end of the experiment.

M_{initial} corresponds to 21% of the total initial U in the schist oxide and 24 % in the schist transition. Because SCE data were not available in the gneiss transition, we assumed that M_{initial} corresponded to 24% of the total initial U mass in that column, i.e., an equal proportion to that determined in the schist transition. Inputs of U from other sources, e.g., from kinetic U-bearing mineral dissolution reactions, were neglected.

The concentration of HFO in each column was calibrated by inputting the measured Fe oxide for each column from QEMSCAN analyses from Supplementary Table S1, and multiplying that value by a scaling factor “ F ” ($F < 1$) such that U concentrations in the model reproduced those observed during Phase 1. The ratio of HFO to water in the model was also scaled to match the solid-to-liquid ratio measured during the initial wetting of the columns at cycle 1, assuming that residual water saturation remained constant in the columns throughout the experiment. This water saturation value was 106 mL H₂O/kg rock in the schist oxide column and 98.5 mL/kg rock in the schist transition column. Model outputs tended to overestimate U concentrations early on in Phase 1, when an exponential decline in major solute (sulfate, Ca, alkalinity) and U concentrations was observed, or underestimate U concentrations at late time, after the initial decline in concentrations stabilized (Supplementary Figure S8). As the sequencing experiment began after the end of Phase 1, F was adjusted to better reproduce U concentrations toward the end of Phase 1 rather than at the start of Phase 1. Thus, simulations were conducted at different values of F until the modeled U concentrations provided the best match to measured concentrations between cycle 50 and the start of sequencing experiments (cycle 105 for the schist and cycle 100 for the gneiss). Fits were optimized by minimizing the root-mean-square error (RMSE) of modeled U concentrations in comparison with measured U concentrations, with good agreement produced for all columns (Supplementary Figure S8).

During the HFO calibration procedure, for each Phase 1 sample, the HFO was first conditioned with the effluent solution’s solute composition (Cl, F, alkalinity, sulfate, Al, Ba, Ca, Cu, Fe, Pb, Mg, Mn, Ni, P, K, Si, Na, Sr, Pb, Se), notwithstanding U, which was added at a subsequent step. The HFO solution mixture was forced to match the measured pH for each sample. In a second step, the solution composition and HFO were amended with U, added into the model as Na₂UO₂(CO₃)₂ using the REACTION keyword, and again the pH was forced to match the measured effluent pH. The mass of U that was removed from the system during each cycle (as effluent) was neglected, as it cumulatively represented a minor amount (0.6 to 3.8%) of the total U present in rock at the outset of experiments.

Batch simulations were conducted iteratively for different values of F until the model with the lowest RMSE was determined. The HFO compositions determined by this approach are 21.1 g HFO/L H₂O in the schist oxide, 4.65 g HFO/L H₂O in the schist transition experiment, and 3.29 g HFO/L in the gneiss transition experiment. These HFO concentrations correspond to values of F of 0.08, 0.15, and 0.08, respectively, and they follow the expected trend of higher HFO availability in oxide facies rocks in comparison with less-weathered transition facies rocks.

During the calibration step, it was noted that including aqueous As in the model produced significant differences in modeled U concentrations because As(V) saturated the HFO. When attempting to reproduce the observed $U_{\text{(aq)}}$ concentrations by the HFO calibration procedure described above and with As_(aq) included in the model input, calibrated HFO concentrations had to exceed the equivalent molar abundance of Fe oxides measured via QEMSCAN to produce a good match for $U_{\text{(aq)}}$ concentrations. While the actual role of competitive sorption of As(V) on U(VI) is

uncertain, As was excluded from the model input file on the basis that modeled HFO availabilities could not realistically exceed the measured Fe oxide abundance.

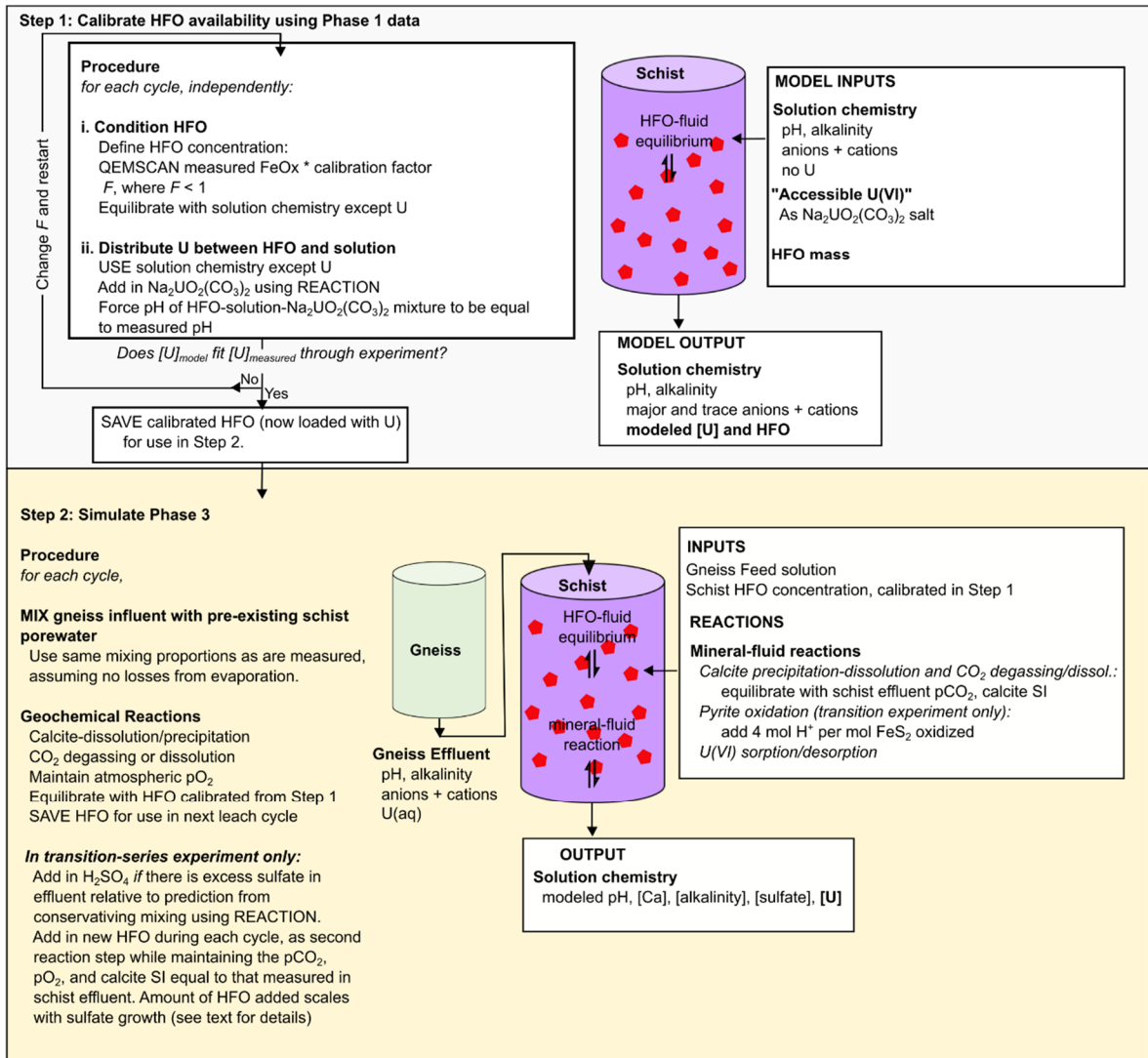


Figure S7. Schematic description of equilibrium sorption modeling of column experiments in PHREEQC. Step 1 was used to calibrate HFO availability in all columns to reproduce available U concentration. In Step 2, these calibrated HFO concentrations were used to simulate Phase 3: influent aqueous chemistry including U was equilibrated with solid-phase HFO composition and calcite, and pyrite dissolution reactions were inferred from effluent sulfate, pCO_2 , and calcite saturation index (SI) values.

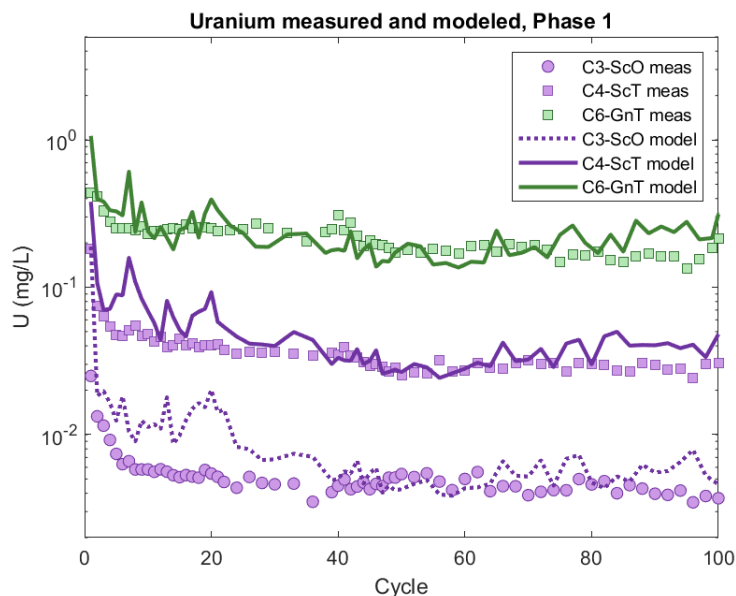
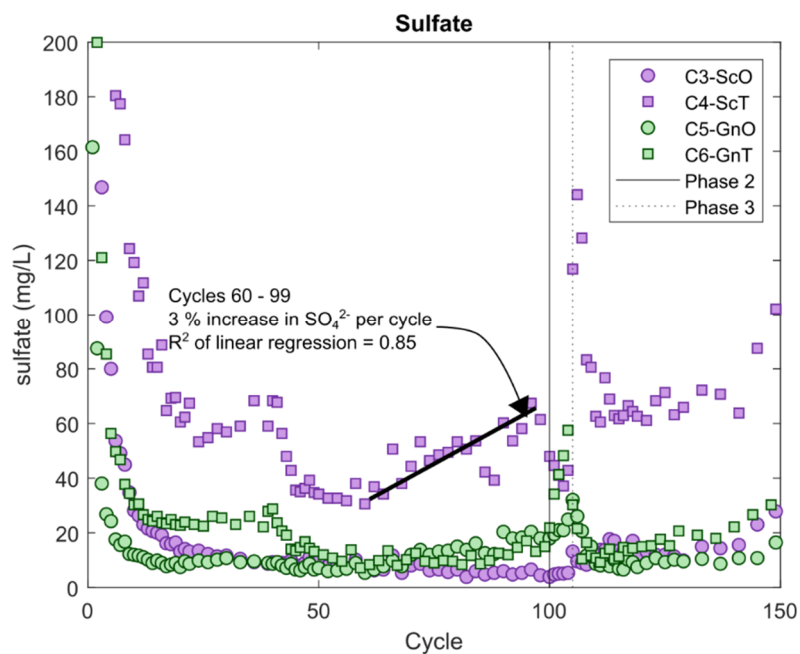


Figure S8. Measured and modeled U concentrations in schist and gneiss effluent during Phase 1 (cycles 1–99).

S4.2 PHREEQC Modeling of Phase 3 Sequencing Experiments

PHREEQC modeling of Phase 3 was conducted as follows. The measured gneiss influent chemistry (pH, Cl, F, sulfate, alkalinity, Al, Ba, Ca, Cu, Fe, Pb, Mg, Mn, Ni, P, K, Si, Na, Sr, Pb, Se, and U) applied to the schist columns at each cycle was allowed to mix with the measured residual porewater in the receiving schist column using the MIX keyword. The amount of residual porewater in the schist was estimated as the difference between influent and effluent volume at each cycle, neglecting water losses due to evaporation, which are expected to be minor at the 4°C experimental temperature. This mixture was allowed to interact with the schist’s HFO surfaces that were calibrated from the Phase 1 aqueous solution chemistry. The HFO was also conditioned to the last schist effluent solution composition (cycle 105) prior to the onset of Phase 3 sequencing experiments. The sources of U in the Phase 3 model are therefore: (i) $U_{(aq)}$ entering the schist column from the gneiss feed solution; (ii) $U_{(aq)}$ already present in the schist column as residual porewater; (iii) U present on the schist’s HFO, as determined from the last HFO solution mixture prior to sequencing experiments (i.e., at cycle 99). The HFO solution batch was forced to match schist effluent calcite saturation indices and pCO_2 (calculated from effluent composition at the subsequent leach cycle) by allowing calcite dissolution-precipitation and CO_2 dissolution-exsolution using the EQUILIBRIUM_PHASES keyword. The batch was also equilibrated with atmospheric pO_2 of 0.21 atm to maintain oxidizing conditions. Homogenous and fully mixed conditions were assumed for the model. Changes in the HFO composition between cycles during Phase 3 were accounted for using the SAVE keyword.

In the schist transition experiment, which contained pyrite (Supplementary Table S4), any excess sulfate in the effluent relative to that predicted from conservative mixing of gneiss influent and residual schist porewater was attributed to pyrite oxidation, which we accounted for in the model by the addition of H_2SO_4 using the REACTION keyword. H_2SO_4 was not added in the schist oxide experiment because of its lower initial sulfide S content and lower dissolved sulfate concentrations suggesting negligible sulfide mineral oxidation (Supplementary Table S1 and Supplementary Figure S9).



Sulfate in Col 4 ScT vs Cycle for Cycles 60 to 99

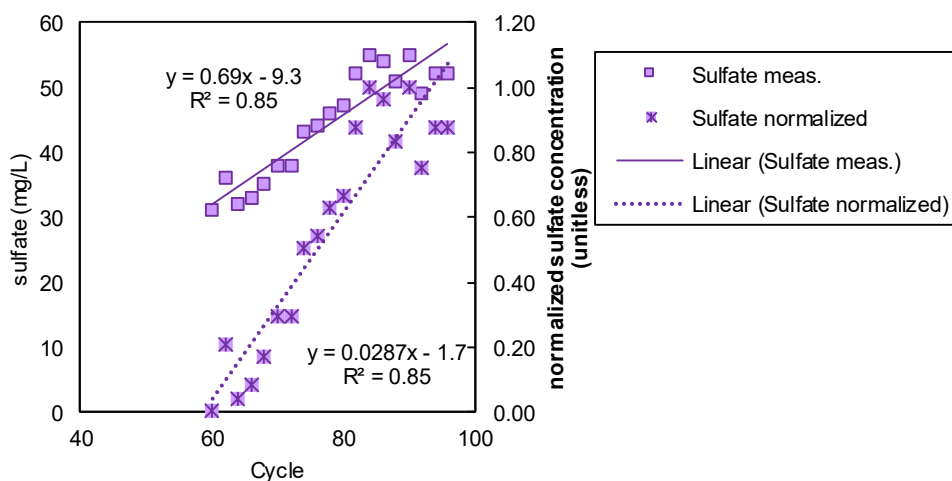


Figure S9. Above: close-up of sulfate concentrations in column experiments showing the initial exponential decline attributed to dissolution of sulfate minerals, and beginning at approximately cycle 50, gradual rise in C4-ScT, which is attributed to kinetic pyrite oxidation. Below: linear regression of sulfate concentrations between cycles 60 and 99 (squares), and sulfate concentrations normalized by the minimum and maximum value between cycles 60 and 99 (crosses). The latter regression corresponds to a 2.87% rise in sulfate concentrations per cycle during this interval.

Publisher's Note: MDPI stays neutral with regard to jurisdictional claims in published maps and institutional affiliations.



© 2020 by the authors. Licensee MDPI, Basel, Switzerland. This article is an open access article distributed under the terms and conditions of the Creative Commons Attribution (CC BY) license (<http://creativecommons.org/licenses/by/4.0/>).